Development of an unresolved CFD-DEM model for the flow of viscous suspensions and its application to solid-liquid mixing

Bruno Blais[a], Manon Lassaigne[a], Christoph Goniva[b], Louis Fradette[a], François Bertrand[a,*]

[a] *Research Unit for Industrial Flow Processes (URPEI), Department of Chemical Engineering, École Polytechnique de Montréal, P.O. Box 6079, Stn Centre-Ville, Montréal,QC, Canada, H3C 3A7*
[b] *DCS Computing GmbH, Altenbergerstraße 66a A-4040 Linz, Austria*

Abstract

Although viscous solid-liquid mixing plays a key role in the industry, the vast majority of the literature on the mixing of suspensions is centered around the turbulent regime of operation. However, the laminar and transitional regimes face considerable challenges. In particular, it is important to know the minimum impeller speed (N_{js}) that guarantees the suspension of all particles. In addition, local information on the flow patterns is necessary to evaluate the quality of mixing and identify the presence of dead zones. Multiphase computational fluid dynamics (CFD) is a powerful tool that can be used to gain insight into local and macroscopic properties of mixing processes. Among the variety of numerical models available in the literature, which are reviewed in this work, unresolved CFD-DEM, which combines CFD for the fluid phase with the discrete element method (DEM) for the solid particles, is an interesting approach due to its accurate prediction of the granular dynamics and its capability to simulate large amounts of particles. In this work, the unresolved CFD-DEM method is extended to viscous solid-liquid flows. Different solid-liquid momentum coupling strategies, along with their stability criteria, are investigated and their accuracies are compared. Furthermore, it is shown that an additional sub-grid viscosity

*Corresponding author
Email address: francois.bertrand@polymtl.ca (François Bertrand)

model is necessary to ensure the correct rheology of the suspensions. The proposed model is used to study solid-liquid mixing in a stirred tank equipped with a pitched blade turbine. It is validated qualitatively by comparing the particle distribution against experimental observations, and quantitatively by compairing the fraction of suspended solids with results obtained via the pressure gauge technique.

Keywords: Solid-liquid mixing; Multiphase flows; Computational Fluid Dynamics; Discrete Element Method; CFD-DEM

1. Introduction and literature review

Solid-liquid mixing plays a key role in the production, transport and homogenization operations inherent to the pharmaceutical, mining, chemical, food processing and cosmetics industries. For these industries, poor mixing can be responsible for large operating costs due to poor yield, over-consumption of energy and product fouling [1]. Solid-liquid mixing has been the subject of considerable work, both experimental (*e.g.* [2–6]) and numerical (*e.g.* [7–13]), but the quasi-totality of it has been centered on the turbulent regime of operation and dilute particle concentrations.

Although this is partially justified by the more common occurrence of turbulent flows in the mixing of suspensions, viscous solid-liquid mixing operations in the transitional and laminar regimes occur frequently in the previously cited industries. These regimes of operation face numerous challenges. For instance, it remains unclear how the rheology of a suspension, the particle-particle interactions and the kinematics of the rotating impeller affect the distribution and dispersion of the solid particles and the flow patterns within the tank.

According to the handbook of industrial mixing [1]:

> *The main objectives of solid-liquid mixing are to create and maintain slurry and/or to promote and enhance the rate of mass transfer between the solid and liquid phases.*

The accomplishment of these objectives is well described by the state (or level) of solid-liquid suspensions: on-bottom, off-bottom, and uniform suspension [1], all of which are illustrated in Figure 1.

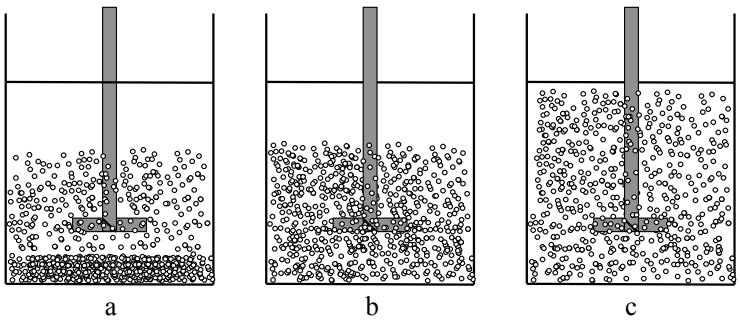

Figure 1: Three levels of suspension: (left) on-bottom suspension, (middle) off-bottom suspension, and (right) uniform suspension. Adapted from [14].

In his 1956 study [15], Kneule identified the state of off-bottom suspension as the optimal operating point. Beyond this level, mass transfer is mainly enhanced by the increased velocity of the fluid and not by an increase of the contact area between the solid and liquid phases. His work was followed by the work of Zwietering [2] who obtained a correlation for the just-suspended speed (N_{js}), which is defined as the minimum impeller speed at which no solid particles rest motionless on the vessel bottom for more than 1 or 2 seconds. The Zwietering correlation is highly limited in the laminar and transitional regimes of operation associated with viscous fluids [14, 16, 17], and for high solid loadings [18]. Other authors have introduced correlations to calculate N_{js}, notably Nienow *et al.* [3], Narayanan *et al.* [4], Baldi *et al.* [5], Mersmann *et al.* [6], but they all share the same limitations to some extent. We refer the reader to Kasat and Pandit [19], and Jafari *et al.* [20] for a review of these correlations.

It must be noted that the experimental results at the basis of the Zwietering correlation, and the majority of the other aforementioned correlations, have been obtained via visual observation. Many alternatives for either direct or indirect measurement of N_{js} exist, as reviewed by Kasat and Pandit [19] and by

Tamburini *et al.* [9]. Among these, a robust way to measure the suspension of particles is the so-called pressure gauge technique introduced by Brucato *et al.* [21] and by Micale *et al.* [22]. This technique was used recently by Lassaigne *et al.* [14] to investigate viscous solid-liquid mixing. Their results indicate that more fundamental work is required to better understand the mechanisms behind the suspension of particles in the laminar and transitional regime, as well as the role of the particle and fluid physical properties.

In light of this review, it is obvious that more work, whether numerical or experimental, is needed to shed light on viscous solid-liquid mixing in order to predict not only the just-suspended speed, but also the local flow characteristics prevailing in the tank. Simulation of such systems may then be used to follow the evolution of both local and global quantities throughout the entire tank. Thus, the development of a robust and efficient computational model would help to a gain deeper insight into the many open issues related to solid-liquid mixing. Numerous models have been designed for solid-liquid flows and each possesses its range of applicability, its strengths and weaknesses. Those applicable to the study of solid-liquid mixing are now reviewed.

1.1. Computational models for solid-liquid flows

Three categories of models are of interest for the study of solid-liquid mixing. They can be distinguished by the scales considered for the representation of each phase (fluid-solid) using the nomenclature proposed by Tsuji [23]: meso-meso, meso-micro, micro-micro.

For micro-micro models, the fluid flow is resolved at a scale smaller than the particle size, and the motion of each particle is tracked. The particle-particle collisions are handled via a method such as the Discrete Element Method (DEM) using either a soft- (DEMs) or hard-collision (DEMh) model. We refer the reader to the papers by Zhu *et al.* [24] or Bertrand *et al.* [25] for a review of the DEM. Such models are referred to as resolved CFD-DEM. In this type of model, the coupling between the two phases results from the application of no-slip boundary conditions on the surface of the particles. A good example of its application to

solid-liquid mixing is given by Derksen [26] where it was used for the study of a small-scale mixing tank containing 3000 particles in the turbulent regime.

Since it resolves the detail of the flow at the particle level, this type of approach is accurate and requires a relatively small number of parameters. However, it suffers from severe limitations in terms of the number of particles it can handle (generally less than 10000) and the scale of the geometries. This is due to the fact that the particle diameter over mesh spacing ratio ($\frac{d_p}{\Delta x}$) must be kept larger than a certain value (such as $\frac{d_p}{\Delta x} > 6$ for the LBM, as noted by ten Cate *et al.* [27], or $\frac{d_p}{\Delta x} > 8$ as found by Hager *et al.* [28]), resulting in untractable numbers of grid cells for the simulation of large industrially relevant geometries. Furthermore, lubrication forces should be added to micro-micro models when particles undergo collisions since the mesh is then unable to resolve the full squeezing flow that results from such collisions. The stability and accuracy of such models remain uncertain for dense solid-liquid flows where particles undergo multiple enduring contacts such as at the start-up of stirred tank mixing operation.

At the other end of the spectrum lies the meso-meso approaches such as the two-fluid model in which both the solid and the fluid phases are considered as interpenetrating continua. This type of model is described in detail in the reference books by Gidaspow [29], Crowe *et al.* [30], Prosperetti and Tryggvason [31] and Ishii and Hibiki [32]. In the context of mixing, it has been used to study solid-liquid systems in the turbulent regime at various concentrations in a wide variety of situations [8–10, 13, 19, 33–42]. A complete overview of the results obtained in these papers would require a review article on its own. Since these results pertain to the turbulent regime and are therefore unrelated to the regime of the present study, we prefer to focus on the limitations and strengths of the meso-meso models.

Because the two-fluid model describes granular matter as a continuum, the computational cost is greatly reduced compared to approaches where each particle is tracked individually. However, the underlying formulation has inherent limitations. First, reproducing the maximal packing fraction of solids re-

quires the addition of either a granular pressure term or an ad-hoc method, to distribute adequately the particles, such as the excess solid volume correction (ESVC) algorithm proposed by Lettieri *et al.* [43]. Secondly, two-fluid models do not allow for scale separation (so-called Burnett or super-Burnett behavior [44]) and predict an instant relaxation of the granular phase, which is invalid in regions of low particle concentrations (dilute or fast granular flows). This has been shown to be highly problematic in situations such as impinging gas-solid flows [45]. This issue can be remedied by using more complex quadrature methods of moment approaches (QMOM) or population balance methods [46], which preserve higher moments of the particle momentum and allow for scale separation, albeit at a higher computational cost.

In between these two classes of approaches lies the meso-micro family of models such as the unresolved CFD-DEM model [24, 47]. In unresolved CFD-DEM, the fluid is solved at a coarser scale than that of the particle using the volume-averaged Navier-Stokes equations (VANS), and the motion of the particles and their collisions are described using DEM (soft or hard). The coupling between the solid and fluid phases is carried out by using explicit expressions for hydrodynamic forces such as drag, lift, etc., the relevance of which depends on the local characteristics of the flow [24].

This method gives a coarser description of the flow field due to the use of volume-averaged equations, yet it can model the granular dynamics with a high degree of fidelity. Consequently, it is valid for all granular regimes and can reproduce characteristics of granular media such as the maximal packing fraction naturally. Since it can handle much larger amounts of particles due to the use of coarser CFD meshes (up to 10^7 [48], or even 10^8 [49]), this model appears as a highly promising candidate for the investigation of mixing in stirred tanks. However, to the best of our knowledge, this method has only been used in the context of gas-solid or solid-liquid flows where the suspending liquid is non-viscous (usually water). Derksen previously proposed and used an unresolved CFD-DEMh for the study of turbulent mixing of dilute suspensions of particles ($< 4vol\%$) where he analyzed the contribution of the lift and drag

hydrodynamic forces to the mixing dynamics and found that the contribution of drag was the dominant one [7]. An improved version of his CFD-DEMh method was recently used to investigate the mixing of dilute bidisperse suspensions by Ayranci *et al.* [50]. However, since this model is based on a hard-sphere DEM, it cannot handle high solids contents or simulate the start-up of a stirred tank. This is not the case for soft-sphere DEM models.

We note that other approaches lie in between the meso-meso and micro-micro descriptions. That is the case for instance of the multiphase particle-in-cell (MP-PIC) [51]. However, they do not reproduce the dynamics of the particles with the same degree of accuracy as unresolved CFD-DEM models.

1.2. Present work

In this work, we present an extension of the unresolved soft-sphere CFD-DEM model for simulating the flow of viscous suspensions. This model is integrated within the CFDEM [52, 53] framework, which combines Open∇FOAM for the CFD part [54] and LIGGGHTS [55, 56] for the DEM part. Firstly, the model is presented in detail along with implicit and explicit momentum coupling strategies. The stability criteria inherent to the model are discussed in the context of a viscous suspending fluid. The advantages and drawbacks of both momentum coupling strategies are also studied via the fluidization of a bed of particles in a viscous fluid. Then, the rheology of the unresolved CFD-DEM model is investigated. Next, the proposed CFD-DEM model is applied to the study of viscous solid-liquid mixing in a stirred tank equipped with a pitched blade turbine (PBT). It is validated against the experimental results of Lassaigne *et al.* [14] by comparing the particle flow patterns and the fraction of suspended particles. Finally, conclusions are drawn on the potential of the model for further investigations.

2. Model Formulation

The CFD-DEM approach consists in using a continuous description for the fluid coarser than the particle scale via the volume-averaged Navier-Stokes equa-

tions while using the discrete element method to model the granular phase accurately. The two models operate independently, but they are coupled at regular intervals, usually with multiple DEM time steps for a single CFD time step. In this section, the equations for each component of the CFD-DEM model used in the present work are described.

2.1. Governing equations for the solid-phase (DEM)

The discrete element method (DEM) bears a high degree of resemblance to molecular dynamics (MD). Both methods are based on the integration of Newton's second law to obtain the evolution in time of the (translational and rotational) velocity and position of the particles.We only give here a brief presentation of the governing equations for the DEM solved using LIGGGHTS, adopting the notation of Zhou *et al.* [47]. For a thorough description, we refer the reader to Bertrand *et al.* [25], Zhu *et al.* [24, 57] and to the LIGGGHTS user manual [55].r

Using Newton's second law of motion, the governing equations for the translational ($\boldsymbol{v}_i$) and rotational ($\boldsymbol{\omega}_i$) motion of a particle i can be written as:

$$m_i \frac{d\boldsymbol{v}_i}{dt} = \sum_j (\boldsymbol{f}_{c,ij}) + \sum_k \boldsymbol{f}_{lr,ik} + \boldsymbol{f}_{pf,i} + \boldsymbol{f}_{g,i} \tag{1}$$

$$I_i \frac{d\boldsymbol{\omega}_i}{dt} = \sum_j (\boldsymbol{M}_{t,ij} + \boldsymbol{M}_{r,ij}) \tag{2}$$

where m_i is the mass of particle i, I_i its moment of inertia, $\boldsymbol{f}_{c,ij}$ the contact force between particles i and j, $\boldsymbol{f}_{lr,ik}$ the non-contact (long-range) forces between particles i and k, $\boldsymbol{f}_{pf,i}$ the particle-fluid interaction forces, $\boldsymbol{f}_{g,i}$ a body force (*e.g* gravity), and $\boldsymbol{M}_{t,ij}$ and $\boldsymbol{M}_{r,ij}$ the tangential and rolling friction moments acting on particles i and j. In the present work, non-contact forces, such as the electrostatic or van Der Waals forces, are not taken into account since they are orders of magnitude smaller than the hydrodynamic or contact forces for the particles considered. The expression for the particle-fluid interaction force depends on which interactions are taken into account (drag, lift, etc.). This is discussed in Section 2.3.

At the core of the DEM lies the contact model for particle-particle interactions. The contact force $\boldsymbol{f}_{c,ij}$ between two particles, which contains both elastic and dissipative forces, is split into two components: normal ($\boldsymbol{f}_{cn,ij}$) and tangential ($\boldsymbol{f}_{ct,ij}$) [24]. This results in the following expressions:

$$\boldsymbol{f}_{c,ij} = \boldsymbol{f}_{cn,ij} + \boldsymbol{f}_{ct,ij} \tag{3}$$

$$\boldsymbol{f}_{c,ij} = -k_{n,ij}\boldsymbol{\delta}_{n,ij} - \gamma_{n,ij}\dot{\boldsymbol{\delta}}_{n,ij} - k_{t,ij}\boldsymbol{\delta}_{t,ij} - \gamma_{t,ij}\dot{\boldsymbol{\delta}}_{t,ij} \tag{4}$$

where $k_{n,ij}$ and $k_{t,ij}$ are the normal and tangential stiffness coefficients, $\gamma_{n,ij}$ and $\gamma_{t,ij}$ the normal and tangential damping coefficients, $\boldsymbol{\delta}_{n,ij}$ and $\boldsymbol{\delta}_{t,ij}$ the normal and tangential particle overlaps, and $\dot{\boldsymbol{\delta}}_{n,ij}$ and $\dot{\boldsymbol{\delta}}_{t,ij}$ their corresponding derivatives with respect to time.

In the present work, the Tsuji model [58] based on the Hertz theory for the normal forces [59, 60] is combined with the Mindlin model for the tangential forces [61, 62]. These models link the stiffness and the damping coefficients to the Young's modulus of the material (Y), its Poisson ratio (ν) and coefficient of restitution (e_r), using the equations in Table 1. Furthermore, the tangential overlap $\boldsymbol{\delta}_{t,ij}$ is limited by Coulomb's law to ensure that $\boldsymbol{f}_{ct,ij} \leq -\mu_{s,ij}\left|\boldsymbol{f}_{cn,ij}\right| \frac{\boldsymbol{\delta}_{t,ij}}{|\boldsymbol{\delta}_{t,ij}|}$.

2.1.1. Determination of the model coefficient

It is readily seen that the DEM model contains numerous parameters, the values of which are not always thoroughly given in the literature. Although their impact is well-established in the context of pure DEM wherein the suspending fluid is neglected, this is not the case for strongly coupled gas-solid and, even more so, solid-liquid flows. For example, it has not yet been established if the coefficient of restitution that is used in solid-liquid flow simulations should be measured using dry particles or if the apparent coefficient of restitution, which decreases significantly as the Stokes number ($St = \frac{\rho_p d_p^2 u_0}{18\mu l_0}$, with u_0 and l_0 characteristic velocity and length respectively) decreases [63], should be used. This is critical, since the latter is flow dependent. In the present work, the parameters taken for each simulation come from Di Renzo and Di Maio [64], Di

Table 1: Equations for the DEM model

Parameter	Equation
Normal stiffness	$k_{n,ij} = \frac{4}{3} Y^*_{ij} \sqrt{R^*_{ij} \delta_{n,ij}}$
Tangential stiffness	$k_{t,ij} = 8 G^*_{ij} \sqrt{R^*_{ij} \delta_{n,ij}}$
Normal damping	$\gamma_{n,ij} = -2\sqrt{\frac{5}{6}} \frac{\ln(e_r)}{\sqrt{\ln^2(e_r)+\pi^2}} \sqrt{\frac{2}{3} k_{n,ij} m^*_{ij}}$
Tangential damping	$\gamma_{t,ij} = -2\sqrt{\frac{5}{6}} \frac{\ln(e_r)}{\sqrt{\ln^2(e_r)+\pi^2}} \sqrt{k_{t,ij} m^*_{ij}}$
Coulomb limit for tangential force	$\boldsymbol{f}_{ct,ij} \leq -\mu_{s,ij} \left\lvert \boldsymbol{f}_{cn,ij} \right\rvert \frac{\boldsymbol{\delta}_{t,ij}}{\lvert \boldsymbol{\delta}_{t,ij} \rvert}$
Torque by tangential forces	$\boldsymbol{M}_{t,ij} = \boldsymbol{r}_i \times (\boldsymbol{f}_{ct,ij})$
Rolling friction torque	$\boldsymbol{M}_{r,ij} = -\mu_{r,ij} \left\lvert \boldsymbol{f}_{cn,ij} \right\rvert \frac{\boldsymbol{\omega}_{ij}}{\lvert \boldsymbol{\omega}_{ij} \rvert} R^*_{ij}$
Equivalent mass	$\frac{1}{m^*_{ij}} = \frac{1}{m_i} + \frac{1}{m_j}$
Equivalent radius	$\frac{1}{R^*_{ij}} = \frac{1}{R_i} + \frac{1}{R_j}$
Equivalent Young's modulus	$\frac{1}{Y^*_{ij}} = \frac{\left(1-\nu_i^2\right)}{Y_i} + \frac{\left(1-\nu_j^2\right)}{Y_j}$
Equivalent shear modulus	$\frac{1}{G^*_{ij}} = \frac{2(2+\nu_i)(1-\nu_i)}{Y_i} + \frac{2(2+\nu_j)(1-\nu_j)}{Y_j}$
Sliding friction coefficient	$\mu_{s,ij}$
Rolling friction coefficient	$\mu_{r,ij}$
Distance to contact point for particle i	$\boldsymbol{r}_i$
Radius of particle i	R_i

Renzo *et al.* [65] and Shao *et al.* [66], which are good examples of work where glass particles were suspended in a liquid. We emphasize that more work would be necessary to shed light on the influence of these parameters on solid-liquid flow behavior.

2.2. Governing equations for the liquid-phase flow (CFD)

In this work, form A (or set II in [47]) of the incompressible volume-averaged Navier-Stokes (VANS) equations is considered for the liquid phase [29]. For a thorough description of the origin of this formulation and its comparison with model B (set I in [47]) and simplified model B (set III in [47]), we refer the reader to Zhou *et al.* [47]. Form A of the VANS equations, which we will simply refer to as the VANS equations in the remainder of this work, is given by:

$$\frac{\partial \epsilon_f}{\partial t} + \nabla \cdot (\epsilon_f \boldsymbol{u}) = 0 \tag{5}$$

$$\frac{\partial (\rho_f \epsilon_f \boldsymbol{u})}{\partial t} + \nabla \cdot (\rho_f \epsilon_f \boldsymbol{u} \otimes \boldsymbol{u}) = -\epsilon_f \nabla p + \nabla \cdot \boldsymbol{\tau} - \boldsymbol{F}_{pf} \tag{6}$$

where ϵ_f is the void fraction, ρ_f the density of the fluid, p the pressure, $\boldsymbol{u}$ the velocity and $\boldsymbol{g}$ the gravity. The viscous stress tensor $\boldsymbol{\tau}$ is defined as:

$$\boldsymbol{\tau} = \epsilon_f \mu \left((\nabla \boldsymbol{u}) + (\nabla \boldsymbol{u})^T - \frac{2}{3} (\nabla \cdot \boldsymbol{u}) \boldsymbol{\delta}_k \right) \tag{7}$$

where μ is the dynamic viscosity and $\boldsymbol{\delta}_k$ is the identity tensor.

The momentum exchange term from the particles to the fluid, $\boldsymbol{F}_{pf}$, is defined as:

$$\boldsymbol{F}_{pf} = \frac{1}{\Delta V} \sum_{i}^{n_p} \boldsymbol{f}_{pf,i} - \boldsymbol{f}_{\nabla p,i} - \boldsymbol{f}_{\nabla \cdot \boldsymbol{\tau},i} - \boldsymbol{f}_{Ar,i} \tag{8}$$

where

$$\boldsymbol{f}_{pf,i} = \boldsymbol{f}_{d,i} + \boldsymbol{f}_{\nabla p,i} + \boldsymbol{f}_{\nabla \cdot \boldsymbol{\tau},i} + \boldsymbol{f}_{Ar,i} \boldsymbol{f}_{\mathrm{vm},i} + \boldsymbol{f}_{B,i} + \boldsymbol{f}_{\mathrm{Saff},i} + \boldsymbol{f}_{\mathrm{Mag},i} \tag{9}$$

and where n_p is the number of particles, ΔV the volume of the cell in which particle i lies and $\boldsymbol{f}_{pf,i}$ is the sum of all fluid-solid interaction forces involving particle i: drag ($\boldsymbol{f}_{d,i}$), pressure gradient ($\boldsymbol{f}_{\nabla p,i}$), viscous stress (or shear

stress) ($\boldsymbol{f}_{\nabla\cdot\boldsymbol{\tau},i}$), Archimedes force ($\boldsymbol{f}_{Ar,i}$), virtual mass ($\boldsymbol{f}_{\mathrm{vm},i}$), Basset force ($\boldsymbol{f}_{B,i}$), Saffman lift ($\boldsymbol{f}_{\mathrm{Saff},i}$) and Magnus lift ($\boldsymbol{f}_{\mathrm{Mag},i}$). We note that the pressure gradient and viscous forces are applied to each particle on an individual basis, but that they manifest themselves directly in the VANS equations, contrary to the other forces which are regrouped within the source term $\boldsymbol{F}_{pf}$. This is the key distinction between models A and B [47] because it changes the pressure equation within the predictor-corrector scheme. This has consequences on the possible loss of hyperbolicity of model A, a phenomenon discussed in the books by Gidaspow [29] and Prosperetti and Tryggvason [31].

In the present work, Equations (5) and (6) are solved using a pressure implicit with splitting of operators (PISO) scheme [67] that was recently extended to the VANS equations. This scheme is described in detail and verified using the method of manufactured solutions by Blais and Bertrand [68]. Using an order of convergence analysis, we showed that the scheme was second-order accurate in space and time for both pressure and velocity. A second-order implicit backward time integration scheme and centered gradient and interpolation schemes are also used here, thus preserving the second-order accuracy for pressure and velocity.

2.3. Governing equations for the solid-liquid coupling strategy

In CFD-DEM, an expression for each force entering into the solid-liquid coupling strategy must be given. Only the drag, pressure and viscous (shear) forces are taken into account in this work. The expressions for these forces are given in Table 2.

The pressure and viscous (shear) forces are needed because, with the unresolved approach, the particles are not discretized explicitely in the CFD part. More precisely, as demonstrated by Crowe *et al.* [30], expressions for these forces can be obtained by integrating the pressure gradient (and the divergence of the shear stress) over the volume occupied by each of these particles. These forces should not be confused with the viscous and pressure components of the drag force, both of which are taken into account by the drag model.

In this work, the Rong drag model [69] is used because of its accuracy over a large range of Reynolds numbers and void fractions. This drag term was derived via DNS simulations carried out with the Lattice Boltzmann method over a large range of solid packings obtained using the DEM. The minimum void fraction investigated by the authors was $\epsilon_f = 0.37$, which means that the Rong drag model is accurate from this situation to very dilute cases ($\epsilon_f \to 1$).

Lift forces, virtual mass and Basset forces are not considered due to the very small relative velocity between the viscous fluid and the particles, and the very low particle relaxation time ($\tau_p = \frac{d_p^2 \rho_p}{18\mu}$).

Table 2: Expressions for the forces taken into account in the CFD-DEM model, for particle i moving at velocity $\boldsymbol{v}_i$ in the solid-liquid coupling strategy on a particle i

Force	Equation
Pressure gradient [24]	$-\frac{\pi}{6} d_{p,i}^3 \nabla p$
Viscous force [24]	$-\frac{\pi}{6} d_{p,i}^3 \nabla \cdot \boldsymbol{\tau}$
Drag - Rong model [69]	$\frac{1}{8} C_D d_{p,i}^2 \rho_f \left\|\boldsymbol{u} - \boldsymbol{v_i}\right\| (\boldsymbol{u} - \boldsymbol{v}_i) \, \epsilon_f^{2-\beta(\epsilon_f, Re_p)}$
	with $C_D = \left(0.63 + \frac{4.8}{\sqrt{Re_p}}\right)^2$
	$\beta(\epsilon_f, Re_p) = 2.65(\epsilon_f + 1) - (5.3 - 3.5\epsilon_f)\, \epsilon_f^2 e^{-\frac{\left(1.5 - \log {Re_p}^2\right)}{2}}$
	and $Re_p = \frac{\rho_f d_{p,i} \left\|\boldsymbol{u} - \boldsymbol{v}_i\right\|}{\mu}$

2.3.1. Calculation of the void fraction and momentum exchange term for the liquid phase flow (CFD)

In this work, two-way coupling is carried out by projecting the volume of the particles and the solid-fluid forces onto the CFD mesh in order to calculate the void fraction ϵ_f and the momentum exchange term $\boldsymbol{F}_{pf}$. Although details on this step are often overlooked in the literature, it must be carried out with care to ensure mass conservation and minimize the occurence of discontinuities for ϵ_f and $\boldsymbol{F}_{pf}$. The naive approach consisting in locating the particles using the position of their centroid has been reported to lead to significant discontinuities and potential instabilities when grid size $\Delta x < 3d_p$ [70, 71].

In the present work, we use the so-called divided approach of the CFDEM

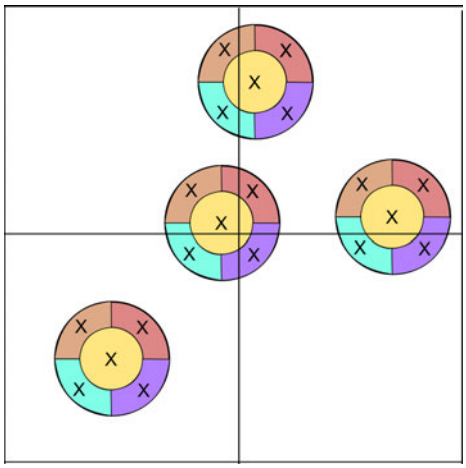

Figure 2: 2D simplified illustration of the divided approach for the projection of particles onto a CFD grid.

framework. It subdivides the projected particle into 27 regions of equal volumes, each of which is represented by a point that is located on the mesh in order to calculate the void fraction and the momentum exchange term. This approach has the significant advantage of being mass conservative while smoothing the void fraction and the momentum exchange term. This is illustrated in Figure 2 on a simplified 2D representation with 5 points (or regions) per particle.

2.3.2. Momentum exchange strategies

Two strategies may be distinguished to apply the momentum exchange force ($\boldsymbol{F}_{pf}$). The simplest one is to add this force directly to the momentum equation as an explicit source term, as in (6). As we will show later, this strategy comes with its own stability criterion. A secondary strategy is to apply this force while taking into account the relative velocity between the solid and fluid phases, leading to:

$$\frac{\partial\left(\rho_f \epsilon_f \boldsymbol{u}\right)}{\partial t} + \nabla \cdot \left(\rho_f \epsilon_f \boldsymbol{u} \otimes \boldsymbol{u}\right) = -\epsilon_f \nabla p + \nabla \cdot \boldsymbol{\tau} + \rho \epsilon_f \boldsymbol{g} + K_{pf}\left(\boldsymbol{u_p} - \boldsymbol{u}\right) \quad (10)$$

where $\boldsymbol{u}_p$ is the particle average velocity within the corresponding grid cell and K_{pf} is a scalar used to scale the magnitude of the momentum exchange force:

$$K_{pf} = \frac{|\boldsymbol{F}_{pf}|}{|\boldsymbol{u}_p - \boldsymbol{u}|} \tag{11}$$

The underlying assumption of this approach is that this force is co-linear with the relative velocity ($\boldsymbol{u_p} - \boldsymbol{u}$), which makes it suitable for implicit coupling strategies.

2.3.3. Smoothing of the momentum exchange force and of the void fraction

Even if the divided approach that projects the particles onto the CFD mesh implicitly smooths the void fraction and the momentum exchange force to a relatively large extent, additional smoothing may be necessary to stabilize the particle-fluid coupling. Various strategies have been reported by Pirker *et al.* [71], such as isotropic diffusive smoothing or the particle cloud and the "darning socks" models. It was shown by this group that both isotropic diffusive smoothing and the "darning socks" model could be efficient for discrete element simulations. In the present work, isotropic diffusive smoothing is applied on the void fraction (ϵ_f) and the momentum exchange force using a parabolic filter. For a given variable $\boldsymbol{\xi}$, this entails solving:

$$\frac{\partial \boldsymbol{\xi}}{\partial t} = \nabla^2 \left(\frac{\lambda^2}{\Delta t_{CFD}} \boldsymbol{\xi} \right) \tag{12}$$

where λ is a characteristic smoothing length and Δt_{CFD} the time step used to solve CFD equations (5) and (6). This smoothing method is chosen because it is conservative, easy to implement and can be easily controlled via the smoothing length λ. In this work, a smoothing length of $\lambda = 2d_p$ was found to be sufficient to improve the stability of all simulations.

2.4. Rotating geometries

Rotating geometries inherent to the stirred tanks investigated in this work are handled using the semi-implicit immersed boundary method (PISO-IB) previously introduced by Blais *et al.* [72]. We refer the reader to this latter paper

for a description of the underlying scheme, its verification and validation in the context of single-phase mixing. This scheme was seamlessly integrated within the CFDEM framework.

3. Stability Analysis of the Model

Four numerical stability criteria are inherent to the two-way coupling unresolved CFD-DEM model proposed in this work.

For the CFD part, if an implicit scheme is used for the viscous component of the VANS equations, the Courant-Friedrich-Lewy (CFL) condition leads to [73] :

$$CFL = \Delta t_{CFD} \max\left(\frac{|\boldsymbol{u}|}{\Delta x}\right) < 1 \tag{13}$$

The definition of a stability criterion for the DEM is more arduous due to the possibility of multiple collisions and the non-linearity of the inherent Hertz collision model. In the present work, the time step for a stable DEM scheme is taken as a fraction of the Rayleigh time step:

$$\Delta t_{DEM} = \alpha \Delta t_{Ra} = \alpha \frac{\Pi}{2} d_p \sqrt{\frac{\rho_p}{G}} \left(\frac{1}{0.1631\nu + 0.8766}\right) \tag{14}$$

where α is a constant lower than unity and $G = \frac{Y}{2(2+\nu)(1-\nu)}$ is the shear modulus (with Y the Young's modulus and ν the Poisson ratio). Different choices have been made for α, such as 0.5 [74], 0.4 [66, 75], 0.1 [76, 77]. Here, a conservative value of $\alpha \leq 0.15$ is taken to ensure stability. We note that alternative stability criteria have been proposed based on the characteristic frequency of the spring [78] or a unit cell approach using the eigenvalues of the stiffness and mass matrices related to multiple collisions [79].

The stability of the fluid-solid coupling step, that is of the impact of the fluid on the DEM equations describing the motion of each individual particle, is linked to the particle relaxation time. By neglecting all solid-fluid forces in Eq. (9) except for drag ($\boldsymbol{f}_{d,i}$) and by assuming an explicit scheme such as the Euler scheme, one can then derive the following stability criterion by analyzing

the amplification factor of the discrete equations:

$$\Delta t_{fp} \leq \frac{4}{3}\frac{d_p \rho_p}{C_d \rho_f}\frac{1}{|\boldsymbol{u}-\boldsymbol{v}_i|} \tag{15}$$

For a single isolated particle in the limit of Stokes flow ($C_D = \frac{24}{Re_p}$), the stability criterion reduces to the particle relaxation time: $\Delta t_c < \frac{d_p^2 \rho_p}{18\mu}$. Taking into account the hindering effect of the surrounding particles via the term $\epsilon_f^{2-\beta(\epsilon_f, Re_p)}$ in the drag model (Table 2) can greatly decrease the value of Δt_{fp} by a factor up to 50.

In the case of an explicit solid-fluid coupling, the action of the drag force on the fluid is also subject to a stability constraint that can be calculated using the relative inertia of the two phases within a finite volume cell, which leads to :

$$\Delta t_{pf} \leq \frac{4}{3}\frac{\epsilon_f}{(1-\epsilon_f)}\frac{d_p}{C_d}\frac{1}{|\boldsymbol{u}-\boldsymbol{v}_i|} \tag{16}$$

This criterion becomes limiting in cases where $\frac{\epsilon_f}{1-\epsilon_f} << 1$ such as in a dense particle bed. However, this issue can be resolved by resorting to an implicit momentum coupling. In practice, the coupling time step (Δt_c) for the two-way coupling must satisfy:

$$\Delta t_c \leq \min\left(\Delta t_{pf}, \Delta t_{fp}\right) \tag{17}$$

In this work, Δt_{CFD} is taken equal to Δt_c and satisfies both (13) and (17).

4. Comparison of the Coupling Strategies

In this section, we compare the stability and precision of the implicit and explicit coupling strategies for the case of a viscous liquid. This is achieved via a simple test-case, which consists in the fluidization of a bed of particles.

4.1. Presentation of the fluidization test case

This case consists of a cylinder, at the bottom of which a bed of particles is initially at rest. At the bottom of this cylinder, a constant velocity inlet U is applied to the fluid whereas a constant pressure boundary condition is

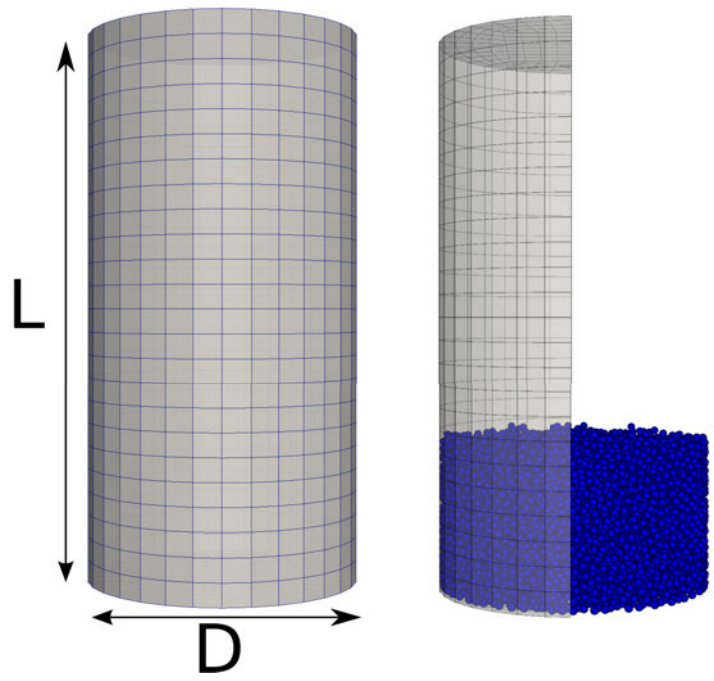

Figure 3: Geometry, mesh and initial configuration of the particles for the fluidization test case

imposed at the top. Slip boundary conditions are applied on the walls of the cylinder, ensuring that the pressure drop is only due to the apparent weight of the particles. For these particles, the bottom of the cylinder is closed by a solid wall.

The pressure drop in the cylinder can be calculated directly by substracting the average pressure at the top from the average pressure at the bottom. Figure 3 shows the geometry and its initial configuration with the particles at rest. The parameters used for the simulation are presented in Table 3. They were extracted from the work Di Renzo and Di Maio [64], Di Renzo *et al.* [65] and Shao *et al.* [66] for glass beads suspended in a liquid, although the Young's modulus of the particles was decreased in order to relax the Rayleigh time step (Eq. (14)).

By changing the inlet velocity, the stability of the scheme and its accuracy

Table 3: Parameters and geometry for the fluidization test case

Particle diameter (d_p)	1 mm
Particle density (ρ_p)	2000 kg.m^{-3}
Young's modulus (Y)	5 MPa
Coefficient of restitution (e_r)	0.9
Poisson ratio (ν)	0.25
Coefficient of friction (μ_f)	0.3
Rolling friction (μ_r)	0.1
DEM time step (Δt_{DEM})	1×10^{-6}s
Liquid density (ρ_f)	1000 kg.m^{-3}
Liquid viscosity (μ)	0.1 Pa.s
CFD time step(Δt_{CFD})	5×10^{-6}s
Coupling time-step (Δt_c)	5×10^{-6}s
Diameter of the cylinder (D)	0.028 m
Length of the cylinder (L)	0.055 m
Mesh ($n_r \times n_\theta \times n_z$)	$8 \times 32 \times 24$

in reproducing both the minimum fluidization velocity and the pressure drop across the bed can be assessed. The pressure drop Δp through a bed can be evaluated by the Ergun equation [80]:

$$\frac{\Delta p}{L_b} = 150\frac{(1-\epsilon_f)^2}{\epsilon_f^3}\frac{\mu U}{d_p^2} + 1.75\frac{1-\epsilon_f}{\epsilon_f^3}\frac{\rho u^2}{d_p} \tag{18}$$

where L_b is the length of the bed of particles. From this equation and under the assumption that $Re_p < 1$, which is true in the present case, the minimal fluidization velocity is given by:

$$U_{mf} = \frac{d_p^2\,(\rho_p - \rho_f)\,g\epsilon_f^3}{150\mu\,(1-\epsilon_f)} \tag{19}$$

4.2. Influence of the coupling strategy

The graph in Figure 4 presents the evolution of the pressure drop within the bed as a function of time for a constant inlet velocity of 200μm.s^{-1}, for both the implicit and explicit momentum exchange coupling schemes. One can readily see that the pressure drop for the implicit scheme suffers from very large oscillations whereas these oscillations are significantly dampened when using

an explicit coupling formulation. Note that no oscillations have been observed by Kloss *et al.* [81] and Goniva and Pirker [82] in the case where the fluid is a gas. For the present configuration, the minimal fluidization velocity is very small (100μm.s^{-1}), so that the error inherent to the averaging of the particle velocities, which vary slightly due to particle-particle contacts and interpolation, affect the average particle velocity $\boldsymbol{u}_p$. The magnitude of this error in the particle velocity field is comparable to that of the minimal fluidization velocity. Therefore, owing to the very short relaxation time of these particles, of the order of $10^{-4}s$, the stiff solid-liquid coupling leads to sharp pressure oscillations in the case of the implicit coupling. The velocity fluctuations also result in the violation of the assumption that the drag force is co-linear with the relative velocity, giving rise to a snowball effect on the fluctuations. For the explicit coupling, these issues are non-existent since the particle-fluid force is applied directly without any averaging. However, we do note the presence of slight oscillations, which occur when small clusters of particles undergo significant collisions. The graph of Figure 5 shows that with the explicit momentum coupling, the right pressure drop and minimal fluidization velocity are recovered accurately.

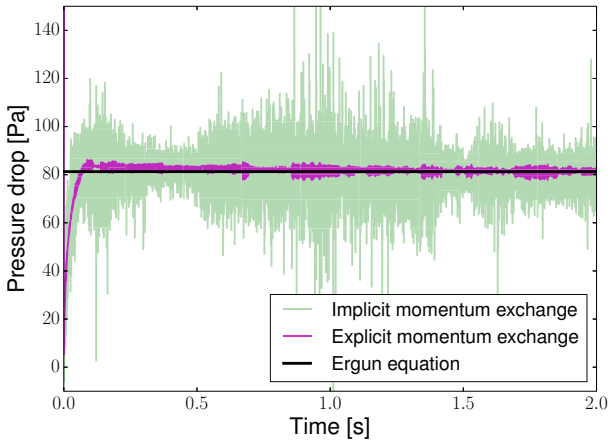

Figure 4: Pressure drop through the cylinder as a function of time for both momentum exchange coupling schemes at a constant inlet velocity of $200\mu\text{m.s}^{-1}$.

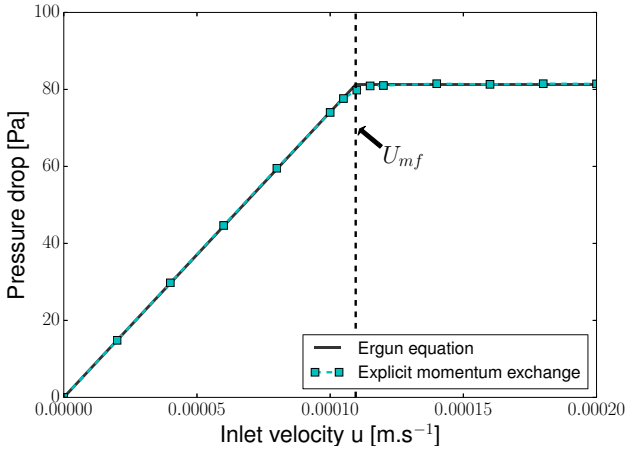

Figure 5: Pressure drop through the cylinder as a function of the inlet velocity.

5. Rheology of the CFD-DEM model

It is well known that at low Reynolds number, the viscosity of a rigid-sphere suspension depends on the volume fraction of the particles [83]. Einstein demonstrated that the relative viscosity(η_r) of a dilute suspension ($\epsilon_p < 5\%$, [84]) in Stokes flow is given by [84]:

$$\eta_r = \frac{\eta_s}{\mu} = 1 + 2.5\epsilon_p \tag{20}$$

where η_s is the apparent viscosity of the suspension, $\epsilon_p = 1 - \epsilon_f$ is the volume fraction of particles.

Einstein reached this result by superimposing the alteration of the velocity field ($\boldsymbol{u}_1$) due to the presence of a single sphere in an infinite medium on top of a constant shear-flow and by integrating the stress due to $\boldsymbol{u}_1$. The seminal paper by Batchelor and Green [85] considered the case of binary interactions to analyze more concentrated suspensions ($\epsilon_p < 10\%$ or $< 15\%$, [84]) and obtained a second-order expression ϵ_s.

For more concentrated suspensions, models have been designed to express the effect of the volume fraction of particles on the viscosity, such as the Kreiger-Dougherty model [86]:

$$\eta_r = \left(1 - \frac{\epsilon_p}{\epsilon_{p,m}}\right)^{-[\eta]\epsilon_{p,m}} \tag{21}$$

where $\epsilon_{p,m}$ is the maximal packing fraction (0.64 for mono-disperse spheres) and $[\eta]$ the intrinsic viscosity (2.5 for spheres).

Although Einstein's results and, to a lesser extent those by Batchelor [85], are not applicable as such for non-dilute concentrations in solid-liquid mixing operations, they indicate that the increase of the viscosity of a suspension is not due to solid-fluid forces such as drag *per se*, but is caused by an increased viscous dissipation in the fluid due to flow disturbances caused by the presence of the particles. This phenomenon happens at the particle and sub-particle scales, and cannot, in theory, be reproduced accurately by an unresolved simulation model. To confirm this, simulations of the shear flow between two parallel plates were

carried out with out model at various solids fractions ranging from 0 vol% to 35 vol% using the parameters in Table 4. These parameters were mainly taken from the work of Di Renzo and Di Maio [64], Di Renzo *et al.* [65] and Shao *et al.* [66] for glass beads suspended in a liquid. However, the Young's modulus of the particles was decreased in order to allow for a larger Rayleigh time step (Δt_{DEM}, Eq. (14)). Also note that the density of the particles was matched to that of the liquid. By measuring the viscous dissipation between the plates and the force acting on the moving plate, the relative viscosity of the fluid could be evaluated. To our knowledge, such a test has not been carried out previously in the literature.

Table 4: Simulation parameters for the flow between two parallel plates

Particle diameter (d_p)	400 μm
Particle density (ρ_p)	1000 kg.m^{-3}
Young's modulus (Y)	10 MPa
Coefficient of restitution (e_r)	0.9
Poisson ratio (ν)	0.25
Coefficient of friction (μ_f)	0.3
Rolling friction (μ_r)	0.1
DEM time step (Δt_{DEM})	1×10^{-6}s
Liquid density (ρ_f)	1000 kg.m^{-3}
Liquid viscosity (μ)	0.05 Pa.s
CFD time step (Δt_{CFD})	1×10^{-5}s
Coupling time-step (Δt_c)	1×10^{-5}s
Plate width and depth (L_x,L_y)	0.025 m
Plate gap (L_z)	0.01 m
Plate velocity (V_x)	0.01 m.s^{-1}
Mesh ($n_x \times n_y \times n_z$)	$20 \times 20 \times 10$

The graph in Figure 6 compares the evolution of the relative viscosity η_r predicted by the unresolved CFD-DEM model to that from the Krieger-Dougherty model. It can readily be seen that the CFD-DEM model does not reproduce the rheology of the suspension in such a case. This is coherent with our previous analysis as the increase in viscosity due to hydrodynamics at the particle and sub-particle scales is not resolved by our unresolved model. The literature does

not propose a solution to this problem. In the present work, this is corrected by the introduction of a viscosity model in which the viscosity depends on the local solids fraction ($\epsilon_p = 1 - \epsilon_f$). This can be seen as a viscous analog to the sub-grid closure used in large eddy simulations, as in the Smagorinsky model [87], to resolve sub-grid stresses. This was implemented by modeling the viscosity in the VANS equations as a space- and time-dependent function of the volume fraction of particles in the same fashion as a classical turbulent viscosity model or a rheological model (where μ would be a function of the shear rate). In the present work, the Krieger-Dougherty model (21) is used to obtain the apparent viscosity as a function of the solids concentration. Unsurprisingly, the graph in Figure 6 shows that with the introduction of this viscosity model, the right rheology is recovered. This demonstrates that there is no interaction between the solid-liquid coupling forces and the viscosity model, since the apparent viscosity measured in the simulations matches that of the analytical model.

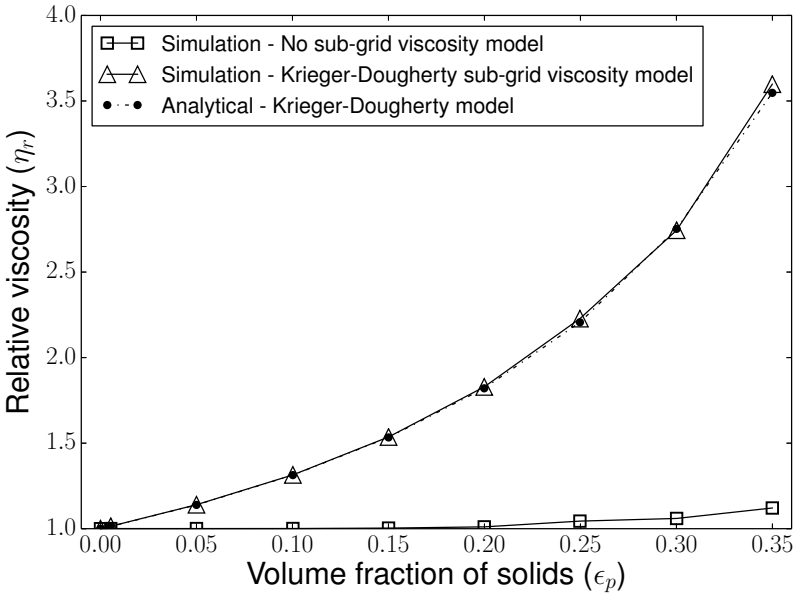

Figure 6: Evolution of the relative viscosity as a function of the volume fraction of solid particles for the unresolved CFD-DEM model, with and without the sub-grid viscosity model, and comparison to the results obtained with the Krieger-Dougherty model.

6. Study of solid-liquid mixing

6.1. Methodology

In this section, the unresolved CFD-DEM model is validated for the case of solid-liquid mixing in the laminar and transitional regimes of operation. We first present the methodology for the experiments and the simulations. Then, we compare the simulation results to experimental data in terms of the flow patterns and fractions of suspended solids. Finally, the simulation results are used to expand our analysis of the solid-liquid mixing in the agitated vessel of this work.

6.1.1. Experimental set-up

The solid-liquid mixing experiments were carried out using glass beads of 3mm diameter at 10 wt% loading in a glucose solution of 1Pa.s viscosity. The properties of both the fluid and the particles are given in Table 5. The set-up, illustrated in Figure 7, consisted in a 0.365m (T) diameter, cylindrical, flat bottomed and unbaffled tank, stirred by a D=T/3 pitched blade turbine that was set at a C=T/4 off-bottom clearance. The dimensions of the experimental rig are summarized in Table 6.

It has been reported that the use of a flat-bottomed tank creates recirculation loops that restrict particle suspension at the wall-to-bottom junction [88]. However, a flat bottom is more suitable for the pressure gauge technique measurement, which is described below. The system was studied without baffles as it has been reported that baffles are not recommended for solid suspensions in viscous fluids because they can cause dead zones and lead to the accumulation of particles [8, 89].

The fraction of suspended solids was obtained experimentally using the pressure gauge technique [14, 21, 22, 40]. The pressure at the bottom of the tank was measured by a pressure sensor supplied by Freescale (MPX5010DP), with a precision of 5%, connected to a small 4 mm hole at the bottom of the tank and protected from particle clogging by a fine mesh, as depicted in Figure 8.

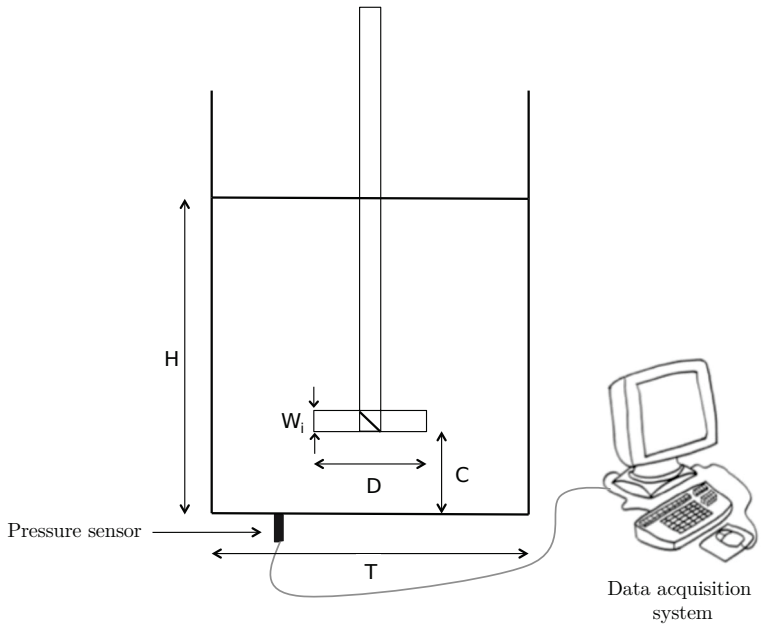

Figure 7: Experimental set-up

Table 5: Physical properties of the fluid and the particles

Symbol	**Name**	**Value**
ρ_f	Density of the fluid	1390 kg.m^{-3}
μ	Dynamic viscosity of the fluid	1 Pa.s
ρ_p	Density of the solid particles	2500 kg.m^{-3}
d_p	Range of diameters for the solid particles	2.66-3.5 mm
$d_{p,32}$	Sauter diameter	3.02 mm
x_s	Mass fraction of solid particles	10 %
ϵ_p	Volume fraction of solid particles	5.8 %

Table 6: Dimensions of the mixing rig

Symbol	Name	Dimension
T	Tank diameter	0.365m
D	Impeller diameter	$\frac{T}{3}$
H	Liquid level	T
C	Off-bottom clearance	$\frac{T}{4}$
W_i	Blade width	$\frac{D}{5}$

During the experiments, the weight of the particles, which are initially held by the tank bottom and lateral walls, is transferred to the fluid as these particles get suspended. This increases the apparent density of the fluid, resulting in an increase of the hydrostatic pressure that is measured by the pressure sensor. This pressure increase is in fact proportional to the fraction of suspended solids. However the dynamic pressure that results from the fluid motion is also felt by the pressure sensor, and thus needs to be removed. Micale *et al.* [22] estimated that beyond N_{js}, only the dynamic component of the total pressure influences the pressure data measurements. Consequently, by fitting a quadratic polynomial to the pressure for large value of N, one can obtain a fit for the dynamic pressure and remove it from the raw pressure results. This produces a corrected curve with a plateau, the onset of which reveals the values of N_{js} and corresponding pressure increase ΔP_{js}. This procedure, with the raw pressure and corrected measurements, is illustrated in Figure 9. The suspended fraction of solids, $X_{suspended}$, can be obtained by plotting the ratio of pressure increase $\frac{\Delta P}{\Delta P_{js}}$ as a function of impeller speed (as in Figure 9). Generally, it can be described by a Weibull function, as noted by Micale *et al.* [22]. In the present work, the experiments were repeated three times to evaluate the uncertainty on the suspended fractions of solids measured by the pressure gauge technique.

6.1.2. Simulation set-up

Simulations were carried out using the unresolved CFD-DEM model presented in Section 2 on the mixing system of dimensions and properties given in

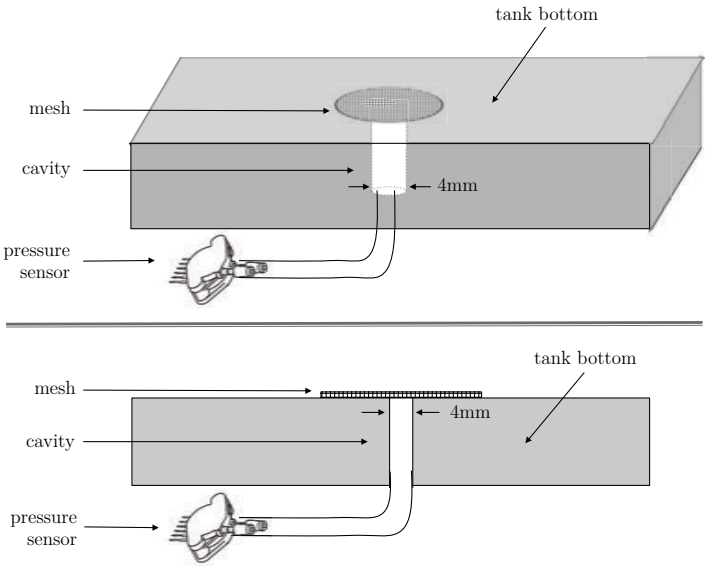

Figure 8: Lateral and oblique views of the pressure sensor at the bottom of the tank

Tables 6 and 5, respectively. Additional model parameters used in the simulations are presented in Table 7. These values were chosen based on the work Di Renzo and Di Maio [64], Di Renzo *et al.* [65] and Shao *et al.* [66] for glass beads suspended in a liquid. The same mechanical properties were given to the tank, the impeller and the particles. To reproduce the size distribution of the particles measured experimentally, 10 different diameters were used. A total of 148 700 particles were required to obtain the desired mass fraction of 10 %.

Table 7: Simulation parameters for the solid-liquid mixing simulation

Young's modulus (Y)	100 MPa
Coefficient of restitution (e_r)	0.9
Poissons ratio (ν)	0.25
Coefficient of friction (μ_s)	0.3
Rolling friction (μ_r)	0.1
DEM time step (Δt_{DEM})	5×10^{-6}s
CFD time step (Δt_{CFD})	1×10^{-4}s
Coupling time-step (Δt_c)	1×10^{-4}s

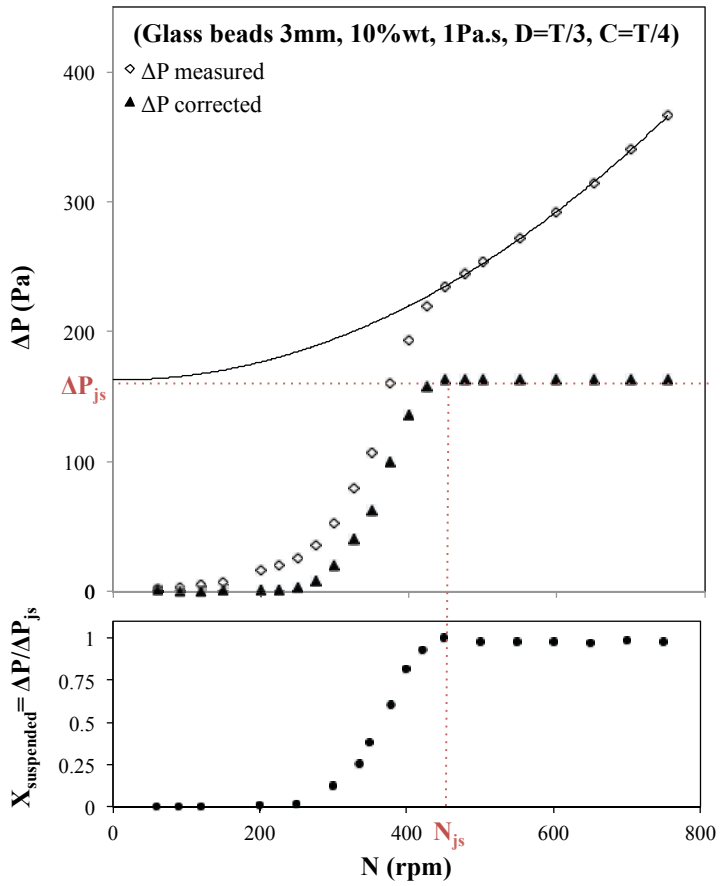

Figure 9: Illustration of the procedure used to obtain the suspension curve from the raw pressure data

Starting with a fully settled bed of particles, obtained via a pure DEM simulation using LIGGGHTS, CFD-DEM simulations were carried out with explicit momentum coupling. The background hexahedral mesh consisted of 33x88x60 (r,θ,z) cells, which was refined in the swept volume of the impeller, thus yielding a total of slightly more than 350k cells. Blais *et al.* [68] found that for this same geometry, more refined meshes did not lead to measurable changes in the torque ($< 1\%$) and the velocity field. A cutoff view of this mesh is presented in Figure 10. The impeller velocity ranged from 100 RPM to 700 RPM (Re=40 to 275), which encompasses the N_{js} value of 425 RPM that was measured experimentally via the pressure gauge technique. The same time step was used for all simulations and the Courant-Friedrichs-Lewy condition (CFL in Eq. (13)) for the simulations at 700 RPM was 0.7. In fact, the solid-fluid coupling criterion (Δt_{pf} in (16)) is the factor that prevented simulations with higher time steps for lower impeller velocities.

For the comparison with the pressure gauge measurements, the simulated pressure was evaluated at the bottom of the stirred tank by averaging its values therein for all cell faces that were comprised within a radius of $0.45R$ to $0.55R$, to comply with the position of the actual pressure sensor. This is illustrated in Figure 11.

It must be noted that the experiments were carefully designed so that they could be reproduced in the simulations, in particular with regards to the number of particles and the stability criteria (more precisely Δt_{fp} and Δt_{pf} in Equations (15) and (16), respectively). However, the relatively high viscosity (1Pa.s) of the fluid entails a fluid-solid stability criterion of $\Delta t_{fp} \leq 1 \times 10^{-3}$s. In the Rong drag model in Table 2, reducing the void fraction ϵ_f increases the value of the drag force, as discussed in Section 3. In the stirred tank, the minimal value that the void fraction ϵ_f can reach is $1 - \epsilon_{p,m} = 0.36$ in regions of maximal packing (the static bed of particles). This leads to a fluid-particle stability criterion of the order of $\Delta t_{fp} \leq 2 \times 10^{-5}$ and, consequently, a solid-fluid stability criterion of $\Delta t_{pf} \leq 7 \times 10^{-6}$ within the bed due to the effect of ϵ_f. This would lead to prohibitively time-consuming simulations.

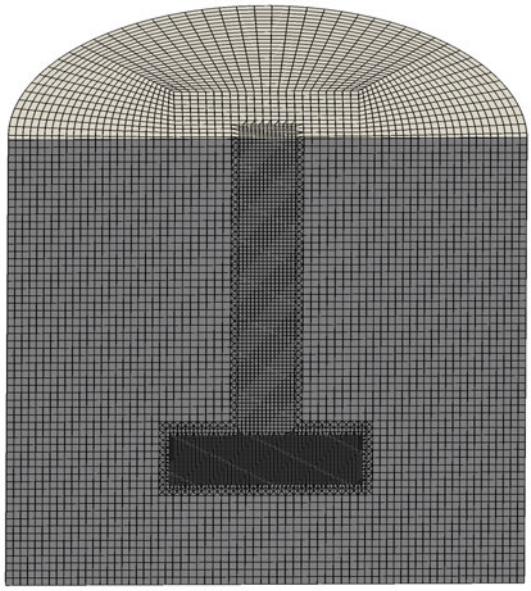

Figure 10: Cutoff view of the CFD mesh

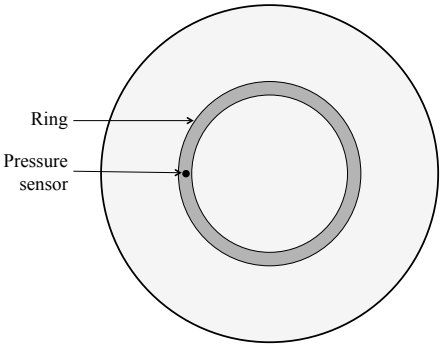

Figure 11: Position of the pressure sensor and ring used to average the simulated pressure results

To resolve this issue, the value of the the void fraction used in the Rong drag equation was limited to $\epsilon_{f,l} = \max(\epsilon_f, 0.8)$, which yields $\Delta t_{pf} \leq 1.0 \times 10^{-4}$. This allowed us to perform 200s of simulation time within a 40-day time frame, instead of the 300 days that would be required without this simplification. The consequence of this is that, in very dense regions ($\epsilon_f < 0.8$) of the tank, the Stokes number was made slightly artificially larger. We recall the definition of the Stokes number:

$$St = \frac{\tau_p}{\tau_f} \tag{22}$$

where $\tau_p = \frac{d_p^2 \rho_p}{18\mu}$ is the particle relaxation time for a single isolated particle and τ_f the fluid relaxation time. In a mixing tank, the shortest relaxation time of the fluid, near the impeller, is proportional to the inverse impeller velocity $\frac{1}{N}$, with N in RPS.

The Stokes number at the largest impeller speed (700 RPM) and for a single particle of the smallest diameter considered ($d_p = 2.66mm$) is $St_m \approx 0.015$. It must be noted that for such a low value of the Stokes number, the particles are expected to behave like passive scalars and thus follow the streamlines, as shown in the simulations of Garg *et al.* [90]. When the Rong drag model dependence on the void fraction is limited, as is proposed here, the particle relaxation time is increased artificially (since the drag force is increased) and so is the Stokes number. However, such limitation of the Rong drag model dependence on ϵ_f does not occur in regions where there is actual flow, but only within quasi-static regions such as in the dense particle bed, at the bottom of the tank, where the local value of the Stokes number is orders of magnitudes lower than St_m. Therefore, this limitation is expected to have no significant impact on the dynamics of the solid-liquid flow within the tank. This was confirmed by carrying out a full simulation at 700 RPM without any limitation on ϵ_f, for which a steady-state could be reached after $20s$ (approximatively 30 days of simulation). This simulation revealed that the simplification had no effect on the particle distribution, and the pressure and velocity fields.

All the simulations were carried out on the Briaree cluster of Calcul Québec.

Each simulation used 2 Intel Westmere processors, each of which consisted of 6 physical cores with a frequency of 2.67 GHz and 12 Go of memory (24 Go total). Each simulation was carried out for 40 days of wall time, resulting in a total consumption of 30 core-years for the 20 impeller velocities investigated.

6.2. Results and discussion

Visual observation of the particle distribution allows for an effective qualitative comparison between experiments and simulations. For $N < 150$ RPM, only a weak displacement of the particles at the top of the bed could be noticed, like a gentle simmer, the energy imparted by the pitched blade turbine being not strong enough to suspend any of them. By increasing the velocity, peculiar flow patterns were triggered for $N \in [150, 250]$. At these velocities, the occurence of a pinching flow was such that particles were initially sucked towards the bottom of the impeller (Figure 12 (I)), which then led to the formation of a cone-shaped (or umbrella-shaped) region below the impeller, isolated from the bulk of the liquid flow (Figure 12 (II)). No significant particle motion across this conical region could be observed. Further increasing the velocity over a critical value of around 300 RPM led to the erosion of the outer part of the bed where particles were lifted close to the wall in a region above the impeller. Once this suspension began, visual observation became difficult due to the opacity of the system. However, it could be noticed both experimentally and from the simulation results that some particles were dragged upward in the near-wall region and downward in the near-shaft region. This comparison, albeit qualitative, showed that the numerical model was able to reproduce the main hydrodynamic transitions and flow patterns that were observed experimentally.

As mentioned in Section 6.1.1, the pressure gauge technique allows for a quantitative determination of the fraction of suspended particles. The graph in Figure 13 shows that a constant pressure at the bottom is reached after 200s for all impeller speeds, although the time required to reach this pressure, which corresponds to the steady-state regime, varies greatly with the impeller speed. This steady-state pressure is the sum of the static pressure due to the

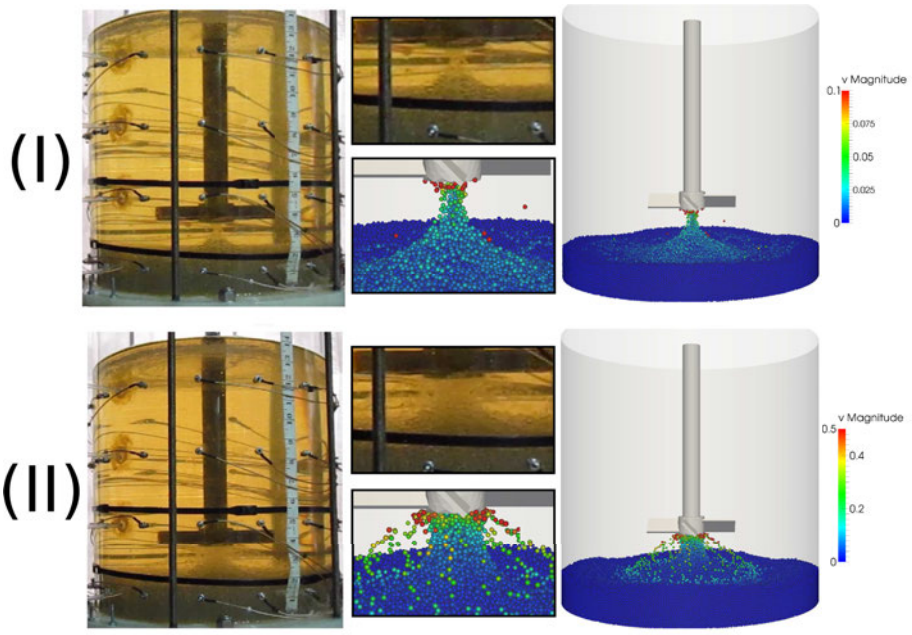

Figure 12: Visual comparison of the behavior of the solid particles in the transitional flow regime for $N = 200$ RPM. (I): Onset of the bed erosion - (II): Formation of a stable cone of particles

increased apparent density and the dynamic pressure. The graph in Figure 14 compares the pressure at the bottom of the tank obtained experimentally to that predicted by our simulation model and averaged using the described in Section 6.1. Although the departure from a zero pressure variation occurs similarly around 300 RPM, the pressure obtained via numerical simulation is larger than the pressure measured experimentally. This is significant for $N \geq N_{js} = 425$ RPM, which corresponds to the speed above which the increase in pressure is solely due to the increase of the dynamic pressure [22]. Note that the time-average value of the pressure was not affected significantly by changes to the size of the ring used in the averaging procedure. This discrepancy can be largely attributed to the set-up used to measure the pressure experimentally (Figure 8). It is measured within a 4 mm hole, which is protected from the particles by a fine mesh. Consequently, the dynamic pressure measured by the probe is significantly underestimated since the flow is damped by the mesh as well as by the presence of a cavity between this probe and the tank. From a practical point of view, both the mesh and the cavity act together as a damper and a low-pass filter for the dynamic pressure. This has the inherent advantage of giving smooth and stable pressure measurements.

Consequently, it is more appropriate to apply the PGT procedure on the two signals and remove the dynamic pressure seperately before comparing the fractions of suspended solids. This is presented in the graph of Figure 15. We note the excellent agreement between the experimental data and simulation results. The transition from a non-suspended to a fully suspended state happens sharply in a small velocity range from 300 to 425 RPM. This transition is subject to larger uncertainties as can be seen by the size of the error bars, compared to those for both the fully unsuspended and suspended states. However, it can be noticed that the simulations estimate accurately, within a 95% confidence interval, the speed at which the suspension of particles is triggered and the just suspended speed, as well as the portion of the curve between these two end points.

The model was also used to investigate the distribution of the solid particles

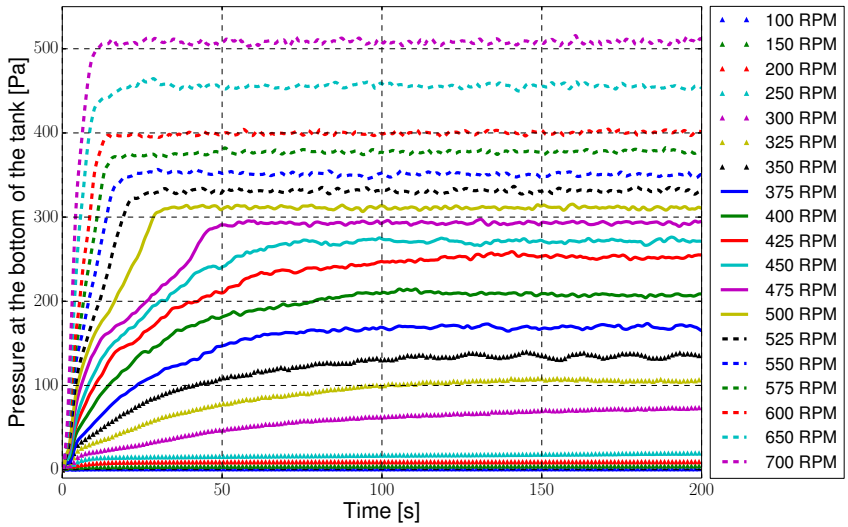

Figure 13: Time evolution of the pressure at the bottom of the tank for various impeller speeds.

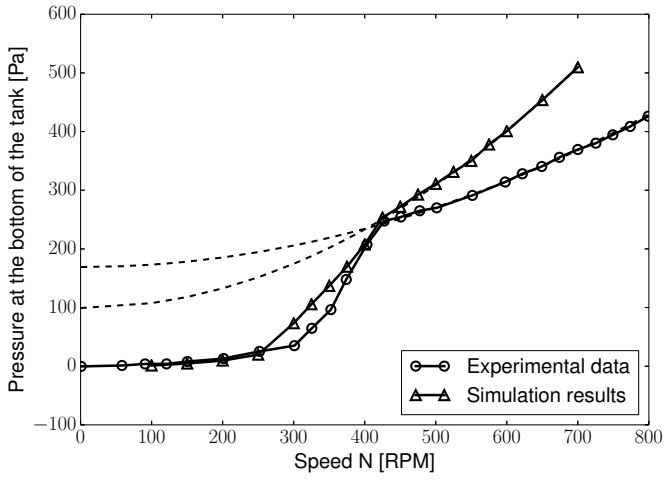

Figure 14: Comparison between the pressure measured experimentally at the bottom of the tank and the simulation results.

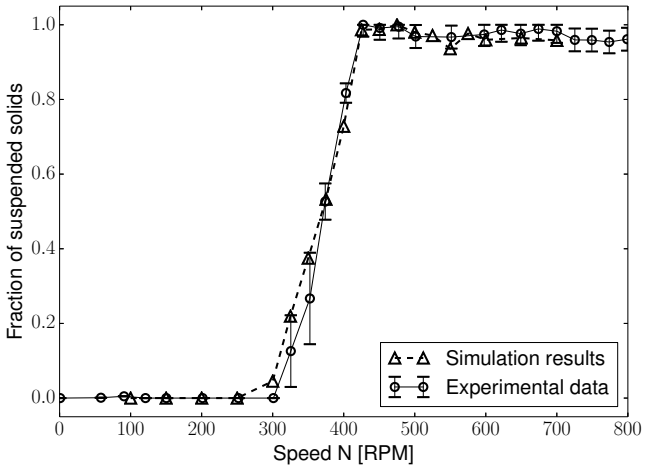

Figure 15: Comparison of the experimental and numerical suspension curves after application of the PGT procedure and the removal of the dynamic pressure component. The error bars represent a 95% confidence interval.

and the flow patterns in the tank. Figure 16 shows the azimuthal average of the void fraction and its standard deviation at 700 RPM, at steady state, which is far above $N_{js} = 425$ RPM. It appears that, although the PGT indicates that all the particles are suspended, there is a small cone-shaped region below the impeller, within which a small fraction of particles ($< 5\%$ of the total mass) remains unsuspended. Such a zone of accumulation of particles in a conical region has already been observed in unbaffled tanks, albeit in the turbulent regime [89]. Such a segregated cone is larger at lower velocity (*e.g.* at 500 RPM), as evidenced in Figure 17. Due to the small total mass of particles contained within this cone and its relatively small erosion with the increase of the impeller speed (as can be seen qualitatively by compairing Figure 17 for 500 RPM and Figure 16 for 700 RPM), its presence is not captured by the PGT.

It is also interesting to note that a low concentration segregated zone of particles, of toroidal shape, is present above the impeller blades at these speeds. Such peculiar patterns have been previously identified by Lamberto *et al.* [91]

and Cabaret *et al.* [92], in the laminar and transitional regimes for PBTs in unbaffled tanks.

Finally, Figure 18 highlights the azimuthal average of the radial, azimuthal and axial components of the liquid velocity within the tank. It can be observed
590 that although the PBT is a mixed discharge impeller, it behaves as a radial discharge impeller for the range of Reynolds numbers considered in this work ($Re \leq 275$, $N \leq 700$RPM). In particular, the poor axial discharge below the impeller is responsible for the formation of the cone of particles therein.

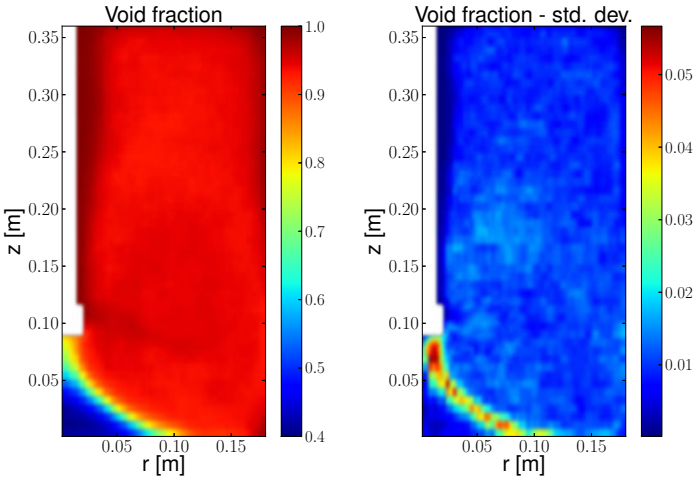

Figure 16: Azimuthal average and standard deviation of the void fraction for $N = 700$ RPM at steady state

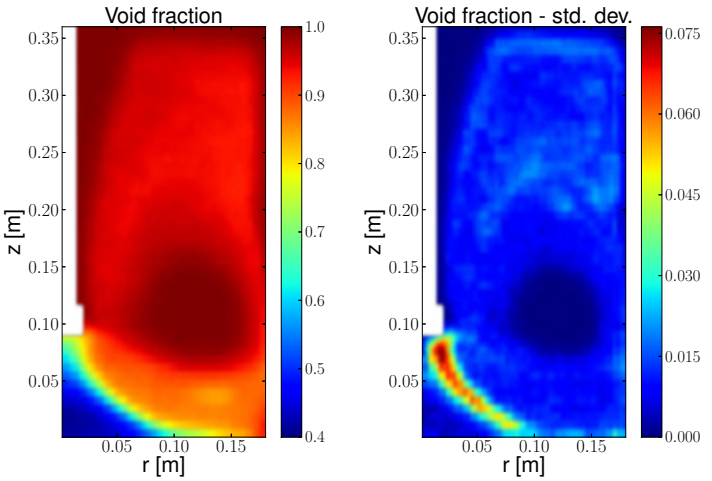

Figure 17: Azimuthal average and standard deviation of the void fraction for $N = 500$ RPM at steady state

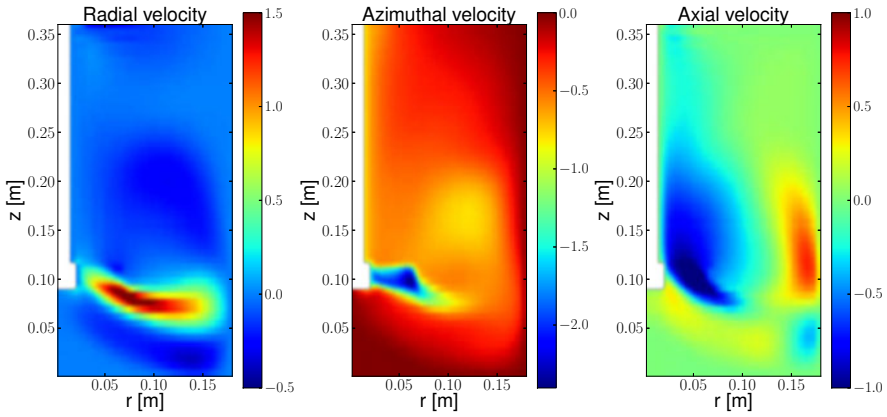

Figure 18: Azimuthal average of the radial, azimuthal and axial components of the liquid velocity for 700 RPM at steady state.

7. Conclusion

The mixing of solid suspensions in the viscous regime is a challenging topic that remains unsolved due to the complex particle-particle and particle-fluid interactions, and the presence of a rotating impeller that generates unsteady 3D flow patterns. Due to its accurate description of the solid phase and computationally tractable description of the fluid, the unresolved CFD-DEM model is a good candidate to the investigation of solid-liquid mixing. However, the validity of this type of approach for viscous suspensions had, to our knowledge, never been assessed.

In the present work, we introduced a CFD-DEM model for viscous suspensions and established stability criteria related to the fluid-fluid, solid-solid, solid-fluid and fluid-solid interactions. Next, we compared implicit and explicit momentum coupling strategies, and showed that in the case of a viscous suspending fluid, the explicit strategy was more accurate in estimating the pressure drop across a bed of particles, mainly due to the significant error introduced by the averaging of the particle velocity within the grid cells. Then, we showed that the apparent rheology of suspensions inherent to the unresolved CFD-DEM model did not reproduce that of a real suspension of particles, which can be attributed to the absence of viscous dissipation at the particle and sub-particle scales. This was remedied by the introduction of a sub-grid viscosity model that brings into play the local void fraction, an approach that is reminescent of the subgrid Smagorinsky-type model used in large eddy simulation.

The unresolved CFD-DEM model for viscous solid-liquid flows developed in this work was used to investigate solid-liquid mixing behavior in a stirred tank equipped with a PBT. Visual observation in the lab showed that the model was able to reproduce the peculiar flow patterns observed when the particles get suspended in the tank. By comparing the fraction of the suspended particles as measured experimentally by the PGT to the pressure averaged at the bottom of the tank in the simulations, we showed that the unresolved CFD-DEM model can predict with excellent accuracy the fraction of suspended particles from the

onset of their suspension to the fully suspended state, thus validating the model in a quantitative manner.

The model was finally used to shed light on the solids distribution and the flow patterns prevailing in the tank. It was found that the PBT behaved like a radial discharge impeller in the laminar and early transitional flow regimes. Even for impeller speeds above the value of N_{js} determined by the PGT, an accumulation of particles within a cone-shaped region below the impeller could be identified, indicating that the suspension could not reach a fully homogenized state. This will be investigated in detail in future work.

This work also opens possibilities for topics related to solid-liquid mixing. In parallel, we are interested in clarifying thoroughly the role of the DEM parameters such as the coefficient of restitution, the coefficients of translational and rolling friction and the Young's modulus on the dynamics of solid-liquid flows.

8. Acknowledgements

The financial support from the Natural Sciences and Engineering Research Council of Canada (NSERC) is gratefully acknowledged. In particular, Bruno Blais is thankful for the NSERC Vanier Scholarship. Computations were made on supercomputer Briaree from the University of Montreal, managed by Calcul Québec and Compute Canada. The operation of this supercomputer is funded by the Canada Foundation for Innovation (CFI), Ministère de l'Économie, de l'Innovation et des Exportations du Québec (MEIE), RMGA and the Fonds de recherche du Québec - Nature et technologies (FRQ-NT). The authors would also like to acknowledge the efficient support from Calcul Québec systems analysts.

References

[1] E. L. Paul, V. A. Atiemo-Obeng, S. M. Kresta, Handbook of Industrial Mixing - Science and Practice (2004).

[2] T. N. Zwietering, Suspending of solid particles in liquid by agitators, Chemical Engineering Science 8 (3) (1958) 244–253.

[3] A. W. Nienow, Suspension of solid particles in turbine agitated baffled vessels, Chemical Engineering Science 23 (12) (1968) 1453–1459.

[4] S. Narayanan, V. K. Bhatia, D. K. Guha, M. N. Rao, Suspension of solids by mechanical agitation, Chemical Engineering Science 24 (2) (1969) 223–230.

[5] G. Baldi, R. Conti, E. Alaria, Complete suspension of particles in mechanically agitated vessels, Chemical Engineering Science 33 (1) (1978) 21–25.

[6] A. Mersmann, F. Werner, S. Maurer, K. Bartosch, Theoretical prediction of the minimum stirrer speed in mechanically agitated suspensions, Chemical Engineering and Processing 37 (6) (1998) 503–510.

[7] J. J. Derksen, Numerical simulation of solids suspension in a stirred tank, AIChE Journal 49 (11) (2003) 2700–2714.

[8] A. Tamburini, A. Cipollina, G. Micale, M. Ciofalo, A. Brucato, Dense solid-liquid off-bottom suspension dynamics: Simulation and experiment, Chemical Engineering Research and Design 87 (4) (2009) 587–597.

[9] A. Tamburini, A. Cipollina, G. Micale, A. Brucato, M. Ciofalo, CFD simulations of dense solid-liquid suspensions in baffled stirred tanks: Prediction of the minimum impeller speed for complete suspension, Chemical Engineering Journal 193 (2012) 234–255.

[10] G. Montante, F. Magelli, Mixed solids distribution in stirred vessels: Experiments and computational fluid dynamics simulations, Industrial & Engineering Chemistry Research 46 (9) (2007) 2885–2891.

[11] N. C. S. Kee, R. B. H. Tan, CFD simulation of solids suspension in mixing vessels, Canadian Journal of Chemical Engineering 80 (4) (2002) 721–726.

[12] F. Wang, Z. S. Mao, X. Q. Shen, Numerical study of solid-liquid two-phase flow in stirred tanks with Rushton impeller - (II) Prediction of critical impeller speed, Chinese Journal of Chemical Engineering 12 (5) (2004) 610–614.

[13] S. Hosseini, D. Patel, F. Ein-Mozaffari, M. Mehrvar, Study of solid-liquid mixing in agitated tanks through computational fluid dynamics modeling, Industrial & Engineering Chemistry Research 49 (9) (2010) 4426–4435.

[14] M. Lassaigne, B. Blais, L. Fradette, F. Bertrand, Experimental investigation of the mixing of viscous liquids and non-dilute concentrations of particles in a stirred tank, Chemical Engineering Research and Design.

[15] F. Kneule, Die prüfung von rührern durch löslichkeitsbestimmung, Chemie Ingenieur Technik 28 (3) (1956) 221–225.

[16] S. B. Ibrahim, A. W. Nienow, The effect of viscosity on mixing pattern and solid suspension in stirred vessels, Eighth European Conference on Mixing (136) (1994) 25–32.

[17] S. Ibrahim, A. W. Nienow, Comparing impeller performance for solid-suspension in the transitional flow regime with Newtonian fluids, Chemical Engineering Research and Design 77 (8) (1999) 721–727.

[18] I. Ayranci, S. M. Kresta, Critical analysis of Zwietering correlation for solids suspension in stirred tanks, Chemical Engineering Research and Design 92 (3) (2014) 413–422.

[19] G. R. Kasat, A. B. Pandit, Review on mixing characteristics in solid-liquid and solid-liquid-gas reactor vessels, Canadian Journal of Chemical Engineering 83 (4) (2005) 618–643.

[20] R. Jafari, P. A. Tanguy, J. Chaouki, Experimental investigation on solid dispersion, power consumption and scale-up in moderate to dense solid-liquid suspensions, Chemical Engineering Research & Design 90 (2) (2012) 201–212.

[21] A. Brucato, G. Micale, L. Rizzuti, Determination of the amount of unsuspended solid particles inside stirred tanks by means of pressure measurements, Récent Progrès Génie des Procédés 11 (1997) 3–10.

[22] G. Micale, F. Grisafi, A. Brucato, Assessment of particle suspension conditions in stirred vessels by means of pressure gauge technique, Chemical Engineering Research and Design 80 (8) (2002) 893–902.

[23] Y. Tsuji, Multi-scale modeling of dense phase gas-particle flow, Chemical Engineering Science 62 (13) (2007) 3410–3418.

[24] H. P. Zhu, Z. Y. Zhou, R. Y. Yang, A. B. Yu, Discrete particle simulation of particulate systems: Theoretical developments, Chemical Engineering Science 62 (13) (2007) 3378–3396.

[25] F. Bertrand, L. A. Leclaire, G. Levecque, DEM-based models for the mixing of granular materials, Chemical Engineering Science 60 (8-9) (2005) 2517–2531.

[26] J. J. Derksen, Highly resolved simulations of solids suspension in a small mixing tank, AIChE Journal 58 (10) (2012) 3266–3278.

[27] A. ten Cate, C. H. Nieuwstad, J. J. Derksen, H. E. A. Van den Akker, Particle imaging velocimetry experiments and lattice Boltzmann simulations on a single sphere settling under gravity, Physics of Fluids 14 (11) (2002) 4012–4025.

[28] A. Hager, C. Kloss, C. Goniva, Towards an efficient immersed boundary method within an open source framework, in: Proc. of 12th International Conference on Multiphase Flow in Industrial Plants, Ischia (Napoli), Italy, 2011.

[29] D. Gidaspow, Multiphase Flow and Fluidization: Continuum and Kinetic Theory Descriptions, Academic press, 1994.

[30] C. Crowe, J. D. Schwartzkopf, M. Sommerfeld, Y. Tsuji, Multiphase Flows with Droplets and Particles Flows, CRC Press, 2012.

[31] A. Prosperetti, G. Tryggvason, Computational Methods For Multiphase Flow, Cambridge University Press, 2007.

[32] M. Ishii, T. Hibiki, Thermo-Fluid Dynamics of Two-Phase Flow, Springer New York, 2011.

[33] G. Micale, G. Montante, F. Grisafi, A. Brucato, J. Godfrey, CFD simulation of particle distribution in stirred vessels, Chemical Engineering Research & Design 78 (A3) (2000) 435–444.

[34] M. Ljungqvist, A. Rasmuson, Numerical simulation of the two-phase flow in an axially stirred vessel, Chemical Engineering Research & Design 79 (A5) (2001) 533–546.

[35] G. Micale, F. Grisafi, L. Rizzuti, A. Brucato, CFD simulation of particle suspension height in stirred vessels, Chemical Engineering Research & Design 82 (A9) (2004) 1204–1213.

[36] G. Montante, F. Magelli, Modelling of solids distribution in stirred tanks: Analysis of simulation strategies and comparison with experimental data, International Journal of Computational Fluid Dynamics 19 (3) (2005) 253–262.

[37] A. Ochieng, A. E. Lewis, CFD simulation of solids off-bottom suspension and cloud height, Hydrometallurgy 82 (1-2) (2006) 1–12.

[38] G. R. Kasat, A. R. Khopkar, V. V. Ranade, A. B. Pandita, CFD simulation of liquid-phase mixing in solid-liquid stirred reactor, Chemical Engineering Science 63 (15) (2008) 3877–3885.

[39] A. Tamburini, A. Cipollina, G. Micale, CFD simulation of solid-liquid suspensions in baffled stirred vessels below complete suspension speed,

ICHEAP-10: 10th International Conference on Chemical and Process Engineering 24 (2011) 1435–1440.

[40] A. Tamburini, A. Cipollina, G. Micale, A. Brucato, M. Ciofalo, CFD simulations of dense solid-liquid suspensions in baffled stirred tanks: Prediction of suspension curves, Chemical Engineering Journal 178 (2011) 324–341.

[41] A. Tamburini, A. Brucato, A. Cipollina, G. Micale, M. Ciofalo, CFD predictions of sufficient suspension conditions in solid-liquid agitated tanks, International Journal of Nonlinear Sciences and Numerical Simulation 13 (6) (2012) 427–443.

[42] A. Tamburini, A. Cipollina, G. Micale, A. Brucato, M. Ciofalo, CFD simulations of dense solid–liquid suspensions in baffled stirred tanks: Prediction of solid particle distribution, Chemical Engineering Journal 223 (2013) 875–890.

[43] P. Lettieri, L. Cammarata, G. Micale, J. Yates, Computational fluid-dynamics simulations of gas fluidized beds using different Eulerian modelling approaches, International Journal of Chemical Reactor Engineering 1 (2003) 1–21.

[44] I. Goldhirsch, Introduction to granular temperature, Powder Technology 182 (2) (2008) 130–136.

[45] X. Chen, J. Wang, A comparison of two-fluid model, dense discrete particle model and CFD-DEM method for modeling impinging gas-solid flows, Powder Technology 254 (2014) 94–102.

[46] D. L. Marchisio, R. O. Fox, Computational models for polydisperse particulate and multiphase systems, Cambridge University Press, 2013.

[47] Z. Y. Zhou, S. B. Kuang, K. W. Chu, A. B. Yu, Discrete particle simulation of particle-fluid flow: model formulations and their applicability, Journal of Fluid Mechanics 661 (2010) 482–510.

[48] P. Pepiot, O. Desjardins, Numerical analysis of the dynamics of two- and three-dimensional fluidized bed reactors using an Euler-Lagrange approach, Powder Technology 220 (2012) 104–121.

[49] J. Capecelatro, O. Desjardins, An Euler–Lagrange strategy for simulating particle-laden flows, Journal of Computational Physics 238 (2013) 1–31.

[50] I. Ayranci, S. M. Kresta, J. J. Derksen, Experiments and simulations on bidisperse solids suspension in a mixing tank, Chemical Engineering & Technology 36 (11) (2013) 1957–1967.

[51] D. M. Snider, An incompressible three-dimensional multiphase particle-in-cell model for dense particle flows, Journal of Computational Physics 170 (2) (2001) 523–549.

[52] CFDEM, CFDEM- Open Source CFD, DEM and CFD-DEM, URL : http://www.cfdem.com, 2015.

[53] C. Goniva, C. Kloss, N. G. Deen, J. A. M. Kuipers, S. Pirker, Influence of rolling friction on single spout fluidized bed simulation, Particuology 10 (5) (2012) 582–591.

[54] OpenCFD, OpenFOAM - The Open Source CFD Toolbox, URL : http://www.openfoam.com, 2014.

[55] LIGGGHTS, LAMMPS Improved for General Granular and Granular Heat Transfer Simulations, URL : hhtp://www.liggghts.com, 2015.

[56] C. Kloss, C. Goniva, LIGGGHTS Open Source Discrete Element Simulations of Granular Materials Based on Lammps, John Wiley & Sons, Inc., 2011, pp. 781–788, (TMS).

[57] H. P. Zhu, Z. Y. Zhou, R. Y. Yang, A. B. Yu, Discrete particle simulation of particulate systems: A review of major applications and findings, Chemical Engineering Science 63 (23) (2008) 5728–5770.

[58] Y. Tsuji, T. Tanaka, T. Ishida, Lagrangian numerical-simulation of plug flow of cohesionless particles in a horizontal pipe, Powder Technology 71 (3) (1992) 239–250.

[59] K. Johnson, Normal contact of elastic solids: Hertz theory, Contact Mechanics (1985) 84–106.

[60] H. Hertz, ber die berhung fester elasticher krpe, Journal fur die reine und angewandte Mathematik (1882) 156–171.

[61] R. Mindlin, H. Deresiewicz, Elastic spheres in contact under varying oblique forces, Journal of Applied Mechanics (1953) .

[62] R. Mindlin, Compliance of elastic bodies in contact, Journal of Applied Mechanics (1949) .

[63] P. Gondret, E. Hallouin, M. Lance, L. Petit, Experiments on the motion of a solid sphere toward a wall: From viscous dissipation to elastohydrodynamic bouncing, Physics of Fluids 11 (9) (1999) 2803–2805.

[64] A. Di Renzo, F. P. Di Maio, Homogeneous and bubbling fluidization regimes in DEM-CFD simulations: Hydrodynamic stability of gas and liquid fluidized beds, Chemical Engineering Science 62 (1-2) (2007) 116–130.

[65] A. Di Renzo, F. Cello, F. P. Di Maio, Simulation of the layer inversion phenomenon in binary liquid-fluidized beds by DEM-CFD with a drag law for polydisperse systems, Chemical Engineering Science 66 (13) (2011) 2945–2958.

[66] T. Shao, Y. Hu, W. Wang, Y. Jin, Y. Cheng, Simulation of solid suspension in a stirred tank using CFD-DEM coupled approach, Chinese Journal of Chemical Engineering 21 (10) (2013) 1069–1081.

[67] R. I. Issa, Solution of the implicitly discretised fluid flow equations by operator-splitting, Journal of Computational Physics 62 (1) (1986) 40–65.

[68] B. Blais, F. Bertrand, On the use of the method of manufactured solutions for the verification of CFD codes for the volume-averaged Navier–Stokes equations, Computers & Fluids 114 (2015) 121–129.

[69] L. W. Rong, K. J. Dong, A. B. Yu, Lattice-Boltzmann simulation of fluid flow through packed beds of uniform spheres: Effect of porosity, Chemical Engineering Science 99 (2013) 44–58.

[70] J. Marshall, K. Sala, Comparison of methods for computing the concentration field of a particulate flow, International Journal of Multiphase Flow 56 (2013) 4–14.

[71] S. Pirker, D. Kahrimanovic, C. Goniva, Improving the applicability of discrete phase simulations by smoothening their exchange fields, Applied Mathematical Modelling 35 (5) (2011) 2479–2488.

[72] B. Blais, M. Lassaigne, C. Goniva, L. Fradette, F. Bertrand, A semi-implicit immersed boundary method and its application to viscous mixing, Accepted to Computers & Chemical Engineering.

[73] J. H. Ferziger, M. Perić, Computational methods for fluid dynamics, Vol. 3, Springer Berlin, 1996.

[74] X. Chen, W. Zhong, X. Zhou, B. Jin, B. Sun, CFD–DEM simulation of particle transport and deposition in pulmonary airway, Powder Technology 228 (2012) 309–318.

[75] A. Hobbs, Simulation of an aggregate dryer using coupled CFD and DEM methods, International Journal of Computational Fluid Dynamics 23 (2) (2009) 199–207.

[76] Y. Xu, K. Kafui, C. Thornton, G. Lian, Effects of material properties on granular flow in a silo using DEM simulation, Particulate Science and Technology 20 (2) (2002) 109–124.

[77] B. Ren, W. Zhong, Y. Chen, X. Chen, B. Jin, Z. Yuan, Y. Lu, CFD-DEM simulation of spouting of corn-shaped particles, Particuology 10 (5) (2012) 562–572.

[78] B. K. Mishra, A review of computer simulation of tumbling mills by the discrete element method: Part i - contact mechanics, International Journal of Mineral Processing 71 (1-4) (2003) 73–93.

[79] F. A. Tavarez, M. E. Plesha, Discrete element method for modelling solid and particulate materials, International Journal for Numerical Methods in Engineering 70 (4) (2007) 379–404.

[80] K. Iinoya, K. Gotoh, K. Higashitani, Powder Technology Handbook, Marcel Dekker, 1991.

[81] C. Kloss, C. Goniva, A. Hager, S. Amberger, S. Pirker, Models, algorithms and validation for open source DEM and CFDDEM, Progress in Computational Fluid Dynamics, an International Journal 12 (2) (2012) 140–152.

[82] C. Goniva, C. Kloss, A. Hager, S. Pirker, An open source CFD-DEM perspective, in: Proceedings of OpenFOAM Workshop, Göteborg, 2010, pp. 22–24.

[83] S. Peker, S. Helvaci, Solid-Liquid Two Phase Flow, Elsevier Science, 2011.

[84] J. Mewis, N. J. Wagner, Colloidal suspension rheology, Cambridge University Press, 2012.

[85] G. Batchelor, J. Green, The determination of the bulk stress in a suspension of spherical particles to order c2, Journal of Fluid Mechanics 56 (03) (1972) 401–427.

[86] I. M. Krieger, T. J. Dougherty, A mechanism for non-Newtonian flow in suspensions of rigid spheres, Transactions of The Society of Rheology (1957-1977) 3 (1) (1959) 137–152.

[87] J. Smagorinsky, General circulation experiments with the primitive equations: I. the basic experiment, Monthly Weather Review 91 (3) (1963) 99–164.

[88] R. N. Sharma, A. A. Shaikh, Solids suspension in stirred tanks with pitched blade turbines, Chemical Engineering Science 58 (10) (2003) 2123–2140.

[89] A. Brucato, A. Cipollina, G. Micale, F. Scargiali, A. Tamburini, Particle suspension in top-covered unbaffled tanks, Chemical Engineering Science 65 (10) (2010) 3001–3008.

[90] R. Garg, J. Galvin, T. Li, S. Pannala, Open-source MFIX-DEM software for gassolids flows: Part I - Verification studies, Powder Technology 220 (2012) 122–137.

[91] D. Lamberto, M. Alvarez, F. Muzzio, Experimental and computational investigation of the laminar flow structure in a stirred tank, Chemical Engineering Science 54 (7) (1999) 919–942.

[92] F. Cabaret, L. Fradette, P. A. Tanguy, New turbine impellers for viscous mixing, Chemical Engineering & Technology 31 (12) (2008) 1806–1815.